Universiteit Antwerpen

Boron structure evolution in magnetic Cr$_2$O$_3$ thin films

Boron Structure Evolution in Magnetic Cr_2O_3 Thin Films

Congli Sun[1,2], Michael Street[3], Chenyu Zhang[4], Gustaaf Van Tendeloo[5], Wenyu Zhao[1,6]*,

Qingjie Zhang[1]

[1]State Key Laboratory of Advanced Technology for Materials Synthesis and Processing, International School of Materials Science and Engineering, Wuhan University of Technology, Wuhan 430070, China
[2]NRC (Nanostructure Research Centre), Wuhan University of Technology, Wuhan 430070, PR China
[3]Department of Physics and Astronomy, Nebraska Center for Materials and Nanoscience, University of Nebraska, Lincoln, Nebraska 68588, USA
[4]School of Applied Engineering Physics, Cornell University, Ithaca, NY, 14850, USA
[5]EMAT (Electron Microscopy for Materials Science), University of Antwerp, Belgium
[6]Foshan Xianhu Laboratory of the Advanced Energy Science and Technology Guangdong Laboratory, Xianhu, 528000, China

*Corresponding authors: Wenyu Zhao (email: wyzhao@whut.edu.cn)

Abstract

B substituting O in antiferromagnetic Cr_2O_3 is known to increase the Néel temperature, whereas the actual B dopant site and the corresponding functionality remains unclear due to the complicated local structure. Herein, A combination of electron energy loss spectroscopy and first-principles calculations were used to unveil B local structures in B doped Cr_2O_3 thin films. B was found to form either magnetic active BCr_4 tetrahedra or various inactive BO_3 triangles in the Cr_2O_3 lattice, with σ^* and π^* bonds exhibiting unique spectral features. Identification of BO_3 triangles was achieved by changing the electron momentum transfer to manipulate the differential cross section for the $1s$-π^* and $1s$-σ^* transitions. Modeling the experimental spectra as a linear combination of simulated B K edges reproduces the experimental π^* / σ^* ratios for 15 to 42 % of the B occupying the active BCr_4 structure. This result is further supported by first-principles based thermodynamic calculations.

KEYWORDS: site-selective doping, magnetic thin films, transition metal oxides, electron

energy loss spectroscopy, density functional theory

With increasing demand on the emergent functionality and growing properties brought by doping, precise manipulating of dopant to occupy specific lattice site is attracting great focus across various research fields. For example, selective enriching of N dopant on the substitutional site leads to a significant increase of the photoelectrochemical activity[1–3]. Rare earth dopants on the substitutional site of 2D transition metal chalcogenides can greatly modulate the optical properties[4–7]. Substituting the host cation in the metal oxides always greatly promotes the surface plasmon[8–11]. Doping on the interstitial sites in semiconductors was reported to substantially modify the electronic and band structures for energy applications[12,13]. With the advanced control of the site-selective doping, unveiling the dopant locations and bonding characteristics is getting increasingly important but also remains as one of the biggest challenges among many analytical techniques[14–20].

Magnetoelectric Cr_2O_3 is the archetypical material for voltage-controlled boundary magnetism. Cr_2O_3 is antiferromagnetic in bulk, but ferromagnetic on the (0001) surface. Switching of the boundary ferromagnetism by magnetoelectric switching of the bulk antiferromagnetic order parameter has been demonstrated[21,22]. Bulk Cr_2O_3 has a Néel temperature of about 307 K, which is too low for microelectronic applications. Increasing magnetic ordering temperature of Cr_2O_3 attracts great interest recently, which is generally achieved by manipulating exchange interaction between neighboring Cr^{3+} ion. One of the prominent methods is through the strain engineering with antiferromagnetic exchange adjusted by the increasing orbital overlapping[23–27]. The strain approach normally requires epitaxial growth of Cr_2O_3 thin films through the lattice mismatch, which is unfavorable for devices and also challenging for the current dielectric deficiency widely observed in epitaxial Cr_2O_3 thin

films[28]. On the other hand, Density functional theory (DFT) calculations predicted that B substituting O to form BCr_4 tetrahedra would increase the exchange energy of neighboring Cr and the Néel temperature[29], which has been confirmed in B-doped Cr_2O_3 thin films[30]. However, the actual B dopant sites and the corresponding magnetic functionality are still unclear.

In this work, a combination of orientation dependent electron energy loss spectroscopy (EELS) and DFT calculations was used to investigate the B-doped Cr_2O_3 film. We found that some B substitutes for O to form BCr_4 tetrahedra, but more of it substitutes for Cr or occupies interstitial sites to create BO_3 triangles. BO_3 triangles are identified by manipulating the direction of the electron momentum transfer in the EELS experiment, which in turn changes the differential cross sections for $1s$-π^* and $1s$-σ^* transitions in B K edges. The functional BCr_4 tetrahedra are identified by distinct K edge features and quantified by modeling the experimental spectra as a linear combination of simulated B K edges. We estimate that 15% - 42% of B occupies magnetically active BCr_4 sites. Details of the film growth, magnetometry measurement, scanning transmission electron microscopy (STEM) sample preparation, DFT calculations, and EELS simulations using FEFF[31] can be found in the supplemental information.

Fig. 1a is a low-angle annular dark field (LAADF) STEM image of the B doped Cr_2O_3/Al_2O_3 film along the $[11\bar{2}0]$ zone axis. Similar c-axis planar boundaries as we reported in undoped Cr_2O_3/Al_2O_3 films[28] still exists, which can be better viewed along the [0001] direction in Fig. 1b. The planar boundary is stabilized by a low interface energy and is not altered by the B doping. Fig. 1c is a high-angle annular dark field (HAADF) STEM image, showing the sharp epitaxial interface and high crystal quality of the Cr_2O_3 film, which also indicates that B doping does not degrade the bulk structure of Cr_2O_3. The HAADF signal scales as Z^a with a ranging from 1.6-1.9, so this image is dominated by high-Z cation sites (Cr in the

film and Al in the substrate). Both O and B atoms are invisible.

To get B dopant signals, EEL spectrum image (SI) was taken with the electron beam along [11$\bar{2}$0] and collection angles at 52-114 mrad. The pixel dwell time was 800 ms, which achieves acceptable signal-to-noise ratio for the B K edge even at low B concentration. No visible electron damage was observed after SI measurements, and EEL SI measurements were conducted on boundary-free areas. A 7×75 pixel SI was acquired covering the whole 80 nm thick Cr_2O_3 film, with the B K edge intensity mapping superimposed that indicates the presence of B inside the whole thickness of the Cr_2O_3 film. The spectrum in Fig. 2 is the B K edge integrated from the Cr_2O_3 film in the SI, with plural scattering removed by Fourier-ratio deconvolution method[32] and background subtracted by the standard power-law model. The averaged B doping level from quantification of the EEL spectra is about 1.2×10^{21} cm^{-3} (~2 % B referred to the number of O atoms), which agrees with the typical B doping levels. The electron dose is ~5×10^6 e/Å^2. To avoid beam damages on the host Cr_2O_3 lattice, we do not perform long EELS acquisition to achieve higher signal to noise ratio. On the other hand, the following linear fitting shows that the EELS simulation error is the major limit to the fitting confidence.

Two primary peaks at 194 eV and 203 eV are typical feature of B sp^2 hybridization, corresponding to 1s-π^* transitions and 1s-σ^* transitions, respectively[33,34]. Similar B K edge feature can also be observed in sp^2 hexagonal BN[35,36]. Due to the significant directionality of unoccupied 2p states of the planar sp^2 structure, B K edges have strong orientation dependence. B K edge taken along [0001] (plan view geometry) is also shown in Fig. 2a. Compared to the [11$\bar{2}$0] spectrum, the [0001] spectrum has significantly smaller π^* / σ^* intensity ratio. This is inconsistent with B substituting for O in BCr$_4$ tetrahedra, with B 2p orbitals in all directions, but consistent with B in BO$_3$ triangles, which have σ bonds in plane and a π bound out of plane[34].

Souche et al. has integrated the angular dependent EELS matrix element to obtain the differential cross section for 1s-π^* transition and 1s-σ^* transition in the B sp^2 geometry, *i.e.*, 2sp$_x$p$_y$ (σ) bonding and p$_z$ (π) bonding, and shown that the σ^* and π^* peak intensities are proportional to the projection of electron momentum transfer $\boldsymbol{q}$ on their corresponding orbital orientations[35]. With the large EELS collection angles used in this experiment (electrons with all momentum transfer are well collected), the orientation dependence in Fig. 2a indicates $\boldsymbol{q}$ has a large projection on the π bonds with incident electron along [11$\bar{2}$0] direction, and $\boldsymbol{q}$ has only a small component on the π bonds when the beam is along [0001]. This indicates the presence of π bonds parallel to the [0001] axis, which is schematically illustrated in Fig. 2b.

DFT calculation was conducted to predict B structures in Cr$_2$O$_3$. All the possible B dopant positions are considered, which in Kroger-Vink notation are B_O, B_{Cr} and B_i, or B substituting for O, B substituting for Cr, and B at an interstitial site. For B_{Cr}, the substituted Cr can either escape the bulk Cr$_2$O$_3$ lattice and migrate to the surface (creating a Cr vacancy), or move to nearby interstitial sites (creating a B_{Cr}-Cr_i Frenkel pair), which implies at least two possible B_{Cr} variants. Possible B pairs are also considered. All of these structures have formation energy difference within ~3 eV under possible experimental chamber oxygen partial pressures, calculated using the Zhang-Northrup formalism[37], following approaches used by Jacobs[38]. This results in 7 potential B dopant structures, as illustrated in Fig. 3. The relaxed B local bonding can be summarized into two categories, as shown in Fig. 3a and Fig. 3b; One is the BCr$_4$ tetrahedra, and the other one is various BO$_3$ triangles with some B slightly shifted out of plane resulting in different bonding angles. All the BO$_3$ triangle structures are normal to the c-axis, which matches with the EELS analysis in Fig. 2.

EELS is simulated from the relaxed dopants models using the multiple-scattering method implemented in the FEFF code[31]. The simulated B K edges of various BO_3 structures have similar characteristics, with two primary peaks at about 194 eV (π) and 203 eV (σ) with the beam along [$11\bar{2}0$] and almost zero 194 eV peaks with the beam along [0001]. Fig. 3c is the simulated EELS for the two typical B structures. The EELS simulations match with Sauer's experimental EELS results[34] on B K edges in various borates and B doped Cr-Fe oxides, in which "fingerprint" 193.6 eV and 204 eV B K edge features were observed in different compounds containing BO_3. In oxides, the excited atom is surrounded by strong backscattering O atoms, so the EELS is dominated by scattering events within the first neighbors of the O. Thus, the near edge features can be explained by a molecular orbital approach. As in the experiments, BCr_4 local bonding can be identified by its distinct π^* / σ^* ratios, especially for [0001] B K edges.

In principle, if the sample contains B in several different sites, the experimental spectrum should be a linear combination of the simulated spectra in Fig. 2. However, attempts to extract the populations of B in various states by direct multiple linear least squares (MLLS) fitting of experimental data to simulated spectra were not satisfactory because the rigid MLLS approach is difficult to reproduce the $\pi^* - \sigma^*$ peak separation difference between EELS experiment and simulation. The background away from the primary π^* and σ^* features is also not well reproduced in the simulations. As π^* / σ^* ratio is strongly correlated with first nearest neighbor of B that represents the local chemical bonding between BCr_4 tetrahedra and BO_3 triangles, we took an alternate approach to quantify the π^* / σ^* ratio in experiment and simulations, then determined the linear combination of simulated spectra which reproduce the intensity ratio of these strongest features in the spectrum. The π^* / σ^* ratio was extracted by fitting Gaussian peaks to the experimental spectra (red dashed lines in Fig. 1). The ratio of the area under π^* Gaussian

g_1 to the area under the σ* Gaussian g_2 is 0.27 and 0.41 for the [0001] EELS and the [11$\overline{2}$0]

EELS, respectively. Fitting the experiment required a third Gaussian at higher energy, g_3, which

is present in the EELS simulations as well. However, the g_3 peak is weak and difficult to

reproduce quantitatively for the multiple scattering EELS simulation method used in this study.

In addition, g_3 is also insensitive to B local structures as well as the magnetic fuctionality, since

the exchange interaction is mainly determined by the nearest neighbors with a strong orbital

overlapping. A similar method was used to obtain the fraction of BO_3 planar rings in complex B

glasses, with the assumption that all the BO_3 structures have the same K edges despite different

bond lengths and bond angles[33,34]. Our EELS calculation in Fig. 3c shows that all the BO_3

have almost the same peak positions, but the relative intensity ratio differs significantly as a

function of B-O bonding angles.

Fig. 4a shows the linear combination weights of the BCr_4 and BO_3 to reproduce the

experimental π* / σ* ratios in both orientations. Spectra of BCr_4 with a tilt BO_3 (#2) and with a

planar BO_3 (#5) are shown in Fig. 4b and Fig. 4c, respectively. All of the possible BO_3 defects

yield acceptable matches to the experimental data, and it is difficult to distinguish them on the

basis of the fine structure. As BCr_4 increases the magnetic exchange interaction of the Cr[29], we

focus on setting bounds on the BCr_4 / total B ratio. The simulation uncertainty is estimated by

comparing the calculated π* / σ* ratios with the experimental π* / σ* ratios based on the well-

defined cubic BN (sp^3) and hexagonal BN (sp^2) structures. Both fitting and simulation

uncertainty were incorporated into the linear combination to get the BCr_4 fitting uncertainty, as

shown in Fig. 4a.

As electron probe is applied for EELS acquisition, channeling effect should be

considered[39,40]. For all the BO_3 triangles, B sits on O columns viewed along the [11$\overline{2}$0]

direction and on Cr columns viewed along the [0001] direction, while for BCr₄, B sits on O columns viewed both on the [11$\bar{2}$0] and [0001] directions. BO₃ has a better electron excitation when electron channels down Cr columns along the [0001] zone axis. Thus, BO₃ fitting weight obtained from [0001] zone axis should be higher than that observed from [11$\bar{2}$0] zone axis, since the channeling difference between the two zones of BCr₄ is not significantly different. This means that both #3 and #5 in Fig. 4a are less likely. Due to the imperfect EELS simulation and fitting uncertainty that incorporated into the linear fitting weights, we are not able to make solid conclusion that completely rule out the possibility of #3 and #5. However, it will significantly narrow down the fitting weights to the overlap area of the two zone axes (green area in Fig. 4a). As a result, the bonds of BCr₄ / total B is 15% to 42%, which means that less than half of B occupies the substitutional site that was predicted to be magnetic functional[29].

To better understand the percentage of each B dopant as a function of experimental conditions, the DFT based thermodynamic model is built, starting from calculating the formation energies according to Zhang-Northrup formalism[37]

$$\Delta E_{form} = E_T^{def,q} - E_T^{perf} - \sum_i \Delta n_i \, \mu_i - \Delta n_e \mu_e \qquad (1)$$

where $E_T^{def,q}$ and E_T^{perf} are total energies of the perfect and B doped supercells, μ_i is the chemical potential of atomic species i. Δn_i is the number of atoms i added to create the dopant. Negative Δn_i represents atoms i removed. Δn_e is the number of electrons added. μ_e is the chemical potential of an electron, which can be defined by choosing a Fermi level E_f within the bandgap relative to the valence-band maximum of the perfect crystal. Here, Total energies $E_T^{def,q}$ and E_T^{perf} is used in place of corresponding free energies, assuming that the vibrational contributions cancel between the perfect and defect cells, and that pressure and temperature dependent terms are negligible for solids.[41]

Chemical potential of O is calculated following the approach used by Lee[42] and takes the form

$$\mu_O^{O_2} = \frac{1}{2}\left[E_{O_2}^{VASP} + \Delta h_{O_2}^0 + H(T,P^0) - H(T^0,P^0) - TS(T,P^0) + kT \ln(\frac{P}{P^0})\right] \tag{2}$$

where $E_{O_2}^{VASP}$ is the T = 0 K total energy of an O_2 gas molecule. $\Delta h_{O_2}^0$ is a numerical correction for the DFT overbinding problem. $H(T^0,P^0)$ and $H(T,P^0)$ are the gas enthalpy at standard and general temperatures $(T^0 = 298.15$ K and $P^0 = 1$ atm). $S(T,P^0)$ is the gas entropy, and $H(T,P^0) - H(T^0,P^0) - TS(T,P^0)$ in Eq. (2) are the free energy per O of O_2 gas relative to the gas enthalpy at T^0 and P^0. The logarithmic term is the adjustment of the chemical potential for arbitrary pressure. These values are obtained experimentally and extrapolated by polynomial fits from Ref 36.[43] $\Delta h_{O_2}^0$ is obtained from fitting experimental formation enthalpy following approach used by Wang.[44] The thermal decomposition of decaborane yields elemental B and H_2 gas under temperature range of 500-1000 °C. The growth temperature is 700 °C. Therefore, the partial pressure of oxygen can be derived from the partial pressure of H_2 and H_2O through the reaction equilibrium $2H_2 + 1O_2 \leftrightarrow 2H_2O$ at 700 °C. As B is solid at 700 °C, H_2 partial pressure is approximated by the measured gas pressure, and H_2O pressure is assumed to be higher than the chamber base pressure (10^{-9} torr). The upper bound of PO_2 is obtained by full decomposition of $B_{10}H_{14}$. With the equilibrium of O between O_2 gas and Cr_2O_3, we can express the relevant Cr chemical potential as a function of Cr_2O_3 cohesive energy and O chemical potential

$$\mu_{Cr}^{Cr_2O_3} = \frac{1}{2}(E_{Cr_2O_3}^{VASP} - 3\mu_O^{O_2}) \tag{3}$$

The calculated formation energy for each B dopant type as a function of Fermi level and charge states are plotted in Fig. 5a, with $\mu_B^{Cr_2O_3}$ referred to solid state B. The concentration of each B dopant type can be expressed as

$$C_i = N_i \exp\left(\frac{-\Delta E_{form}}{K_B T}\right) \tag{4}$$

where N_a is the number of sites per unit volume that the dopant can occupy. Summing the concentration from acceptor-type dopants (negative charge) and donor-type dopants (positive charge) along their compensating electrons and holes gives the condition of charge neutrality:

$$\sum_i C_i q_i = [e^-] - [h^+] \tag{5}$$

where q_i is the charge state for dopant i, $[e^-]$ and $[h^+]$ are electron and hole concentrations determined by bandgap and Fermi level. Eq. (5) is solved following the approach used by Jacobs[38] that yields a single self-consistent value for the Fermi energy and equilibrium that ensures both charge neutrality and electron/hole mass action. Here, we set Eq. (5) as a function of B chemical potentials to match the experiment B doping level C_B:

$$\sum_i C_i = C_B \tag{6}$$

In this way, Fermi level is determined, and the composition of each B dopant structure can be calculated. The result shows an equilibrium Fermi level at 1.69 eV and nearly 100% B occupying B_{Cr} (#5 in Fig. 3) state, which can be readily viewed by a much lower formation energy of B_{Cr}, as it is shown in Fig. 5a. The 100% B_{Cr} does not match the EELS results. Table I is the calculated exchange energies of BO_3 dopants (details of exchange energy calculation can be found in supporting materials). B_{Cr} does not have significant effect on the bulk Cr_2O_3 exchange energy of 120 meV[29]. This means that 100% B_{Cr} also contradicts the increased magnetic ordering temperature in the B doped Cr_2O_3 films (Figure S1 in supplementary information).

Here, we believe that the B_{Cr} state is trapped at one of the $B_{Cr}(Cr_i)$ state (#3 and #4 in Fig. 3), which means that although the formation energy of B_{Cr} is low, the substituted Cr is trapped at the neighboring interstitial sites. This is also reasonable as forming B_{Cr} requires long-

range migration of Cr ion which is always kinetically restricted in solids. The same calculation is done without B_{Cr}, with the calculated ratio of each B dopant plotted as a function of oxygen partial pressure (B dopant with percentage ratio larger than 0.1% is shown) in Fig. 5b. Assuming the complete decomposition of $B_{10}H_{14}$ background gas, the experimental oxygen partial pressure derived from $2H_2 + 1O_2 \leftrightarrow 2H_2O$ equilibrium is 10^{-28} atm, which gives a BCr$_4$ dopant / total B about 50% according to Fig .5b (Oxygen vacancy concentration is less than 0.01% per Cr$_2$O$_3$ unit cell even at 10^{-28} atm oxygen partial pressure. Its effect on the Fermi level is negligible). The effective oxygen pressure can be higher with partial decomposition of $B_{10}H_{14}$ background gas. In addition, although the functional BCr$_4$ dopant would be kinetically maintained after growth (we do not see any significant change of the B K edges for B doped Cr$_2$O$_3$ samples stored in air condition for at least 3 monthes), no BCr$_4$ dopant would exist eventually at the standard equilibrium state. The dynamics of B dopant is out of scope of this study, but both of them makes BCr$_4$ / total B ratio samller than 50%.

These results may shed some light on the difficulty of integrating B-doped Cr$_2$O$_3$ into functioning magnetoelectric devices, due to the thermodynamic restriction. They may also suggest processing paths to make more efficient use of B: suppressing BO$_3$ defects in favor of BCr$_4$ defects should raise the Néel temperature at constant B content or enable similar Néel temperatures to be achieved at lower B content. As shown in Fig. 5b, further decreasing the growth oxygen partial pressure does not significantly increase the functional BCr$_4$ ratio and is also restricted due to the intrinsic stability of Cr$_2$O$_3$ host lattice. Therefore, control of growth kinetics that traps B on the substitutional site as the metastable state is more promising. If thermodynamics is dominating, co-doping with Al is another potential strategy to lower the formation energy of and stabilize the desirable BCr$_4$ defects.[45]

In summary, by a combination of EELS fine structure and DFT simulations, we have shown that B-doped Cr_2O_3 contains more than half of B in BO_3 triangles and 15% - 42% B in the BCr_4 tetrahedra. BO_3 does not increase the exchange coupling. However, the B occupying BCr_4 tetrahedra are sufficient to substantially increase the antiferromagnetic ordering temperature by more than 25%. Recognizing the existence of the BO_3 defects opens pathways to engineering more efficient use of B to increase the Néel temperature.

Data Availability Statement

The authors confirm that the data supporting the findings of this study are available within the article and its supplementary materials.

Reference

[1]   G. Wang, X. Xiao, W. Li, Z. Lin, Z. Zhao, C. Chen, C. Wang, Y. Li, X. Huang, L. Miao, C. Jiang, Y. Huang, X. Duan, Significantly Enhanced Visible Light Photoelectrochemical Activity in TiO_2 Nanowire Arrays by Nitrogen Implantation, Nano Lett. 15 (2015) 4692–4698. doi:10.1021/acs.nanolett.5b01547.

[2]   K.-H. Ye, H. Li, D. Huang, S. Xiao, W. Qiu, M. Li, Y. Hu, W. Mai, H. Ji, S. Yang, Enhancing photoelectrochemical water splitting by combining work function tuning and heterojunction engineering, Nat. Commun. 10 (2019) 3687. doi:10.1038/s41467-019-11586-y.

[3]   G. Zeng, T.A. Pham, S. Vanka, G. Liu, C. Song, J.K. Cooper, Z. Mi, T. Ogitsu, F.M. Toma, Development of a photoelectrochemically self-improving Si/GaN photocathode for efficient and durable H_2 production, Nat. Mater. 20 (2021) 1130–1135. doi:10.1038/s41563-021-00965-w.

[4]   D. Haldar, A. Ghosh, S. Bose, S. Mondal, U.K. Ghorai, S.K. Saha, Defect induced photoluminescence in MoS_2 quantum dots and effect of Eu^{3+}/Tb^{3+} co-doping towards efficient white light emission, Opt. Mater. (Amst). 79 (2018) 12–20. doi:10.1016/j.optmat.2018.03.012.

[5]   G. Bai, S. Yuan, Y. Zhao, Z. Yang, S.Y. Choi, Y. Chai, S.F. Yu, S.P. Lau, J. Hao, 2D Layered Materials of Rare-Earth Er-Doped MoS_2 with NIR-to-NIR Down- and Up-Conversion Photoluminescence, Adv. Mater. 28 (2016) 7472–7477. doi:10.1002/adma.201601833.

[6]   R. Turki, G. Ghimire, K. Damak, H.Y. Song, S. Boandoh, J. Kim, C. Rüssel, R. Aad, J. Kim, R. Maalej, Luminescent Sm-doped aluminosilicate glass as a substrate for enhanced photoresponsivity of MoS_2 based photodetector, Appl. Surf. Sci. 565 (2021) 150342. doi:https://doi.org/10.1016/j.apsusc.2021.150342.

[7]   H. Chen, M. Sun, J. Ma, B. Zhang, C. Wang, L. Guo, T. Ding, Z. Zhang, H. Zheng, H. Xu, Multiplasmons-Pumped Excited-State Absorption and Energy Transfer Upconversion of Rare-Earth-Doped Luminescence beyond the Diffraction Limit, ACS Photonics. 8 (2021)

1335–1343. doi:10.1021/acsphotonics.0c01747.

[8]   O. Zandi, A. Agrawal, A.B. Shearer, L.C. Reimnitz, C.J. Dahlman, C.M. Staller, D.J. Milliron, Impacts of surface depletion on the plasmonic properties of doped semiconductor nanocrystals, Nat. Mater. 17 (2018) 710–717. doi:10.1038/s41563-018-0130-5.

[9]   X. Qin, A.N. Carneiro Neto, R.L. Longo, Y. Wu, O.L. Malta, X. Liu, Surface Plasmon–Photon Coupling in Lanthanide-Doped Nanoparticles, J. Phys. Chem. Lett. 12 (2021) 1520–1541. doi:10.1021/acs.jpclett.0c03613.

[10]   C. Wang, H. Su, J. Zhang, H. Zhao, Surface metallization from ab initio theory and subwavelength coupling via surface plasmon polaritons in Cu-doped lithium niobate/tantalate owing to charge accumulation, Appl. Surf. Sci. 551 (2021) 149294. doi:https://doi.org/10.1016/j.apsusc.2021.149294.

[11]   M. Sygletou, S. Benedetti, A. di Bona, M. Canepa, F. Bisio, Doping-Dependent Optical Response of a Hybrid Transparent Conductive Oxide/Plasmonic Medium, J. Phys. Chem. C. 126 (2022) 1881–1889. doi:10.1021/acs.jpcc.1c07567.

[12]   J. Zhi, M. Zhou, Z. Zhang, O. Reiser, F. Huang, Interstitial boron-doped mesoporous semiconductor oxides for ultratransparent energy storage, Nat. Commun. 12 (2021) 445. doi:10.1038/s41467-020-20352-4.

[13]   Y. Li, C.-K. Peng, H. Hu, S.-Y. Chen, J.-H. Choi, Y.-G. Lin, J.-M. Lee, Interstitial boron-triggered electron-deficient Os aerogels for enhanced pH-universal hydrogen evolution, Nat. Commun. 13 (2022) 1143. doi:10.1038/s41467-022-28805-8.

[14]   W. Zhou, M.D. Kapetanakis, M.P. Prange, S.T. Pantelides, S.J. Pennycook, J.C. Idrobo, Direct determination of the chemical bonding of individual impurities in graphene, Phys.

Rev. Lett. 109 (2012) 2–6. doi:10.1103/PhysRevLett.109.206803.

[15] Y.C. Lin, D.O. Dumcenco, H.P. Komsa, Y. Niimi, A. V. Krasheninnikov, Y.S. Huang, K. Suenaga, Properties of individual dopant atoms in single-layer MoS_2: Atomic structure, migration, and enhanced reactivity, Adv. Mater. 26 (2014) 2857–2861. doi:10.1002/adma.201304985.

[16] U. Bangert, W. Pierce, D.M. Kepaptsoglou, Q. Ramasse, R. Zan, M.H. Gass, J.A. Van den Berg, C.B. Boothroyd, J. Amani, H. Hofsäss, Ion Implantation of Graphene—Toward IC Compatible Technologies, Nano Lett. 13 (2013) 4902–4907. doi:10.1021/nl402812y.

[17] R.J. Nicholls, A.T. Murdock, J. Tsang, J. Britton, T.J. Pennycook, A. Koós, P.D. Nellist, N. Grobert, J.R. Yates, Probing the Bonding in Nitrogen-Doped Graphene Using Electron Energy Loss Spectroscopy, ACS Nano. 7 (2013) 7145–7150. doi:10.1021/nn402489v.

[18] Q.M. Ramasse, C.R. Seabourne, D.-M. Kepaptsoglou, R. Zan, U. Bangert, A.J. Scott, Probing the Bonding and Electronic Structure of Single Atom Dopants in Graphene with Electron Energy Loss Spectroscopy, Nano Lett. 13 (2013) 4989–4995. doi:10.1021/nl304187e.

[19] S. Cheng, G. Yang, Y. Zhao, M. Peng, J. Skibsted, Quantification of the boron speciation in alkali borosilicate glasses by electron energy loss spectroscopy, Nat. Publ. Gr. (2015) 1–7. doi:10.1038/srep17526.

[20] D. Gilks, Z. Nedelkoski, L. Lari, B. Kuerbanjiang, K. Matsuzaki, T. Susaki, D. Kepaptsoglou, Q. Ramasse, R. Evans, K. Mckenna, V.K. Lazarov, Atomic and electronic structure of twin growth defects in magnetite, Nat. Publ. Gr. (2016) 1–8. doi:10.1038/srep20943.

[21] P. Borisov, A. Hochstrat, X. Chen, W. Kleemann, C. Binek, Magnetoelectric Switching of

Exchange Bias, Phys. Rev. Lett. 94 (2005) 117203. doi:10.1103/PhysRevLett.94.117203.

[22] X. He, Y. Wang, N. Wu, A.N. Caruso, E. Vescovo, K.D. Belashchenko, P.A. Dowben, C. Binek, Robust isothermal electric control of exchange bias at room temperature., Nat. Mater. 9 (2010) 579–85. doi:10.1038/nmat2785.

[23] Y. Kota, H. Imamura, M. Sasaki, Enhancement of spin correlation in Cr_2O_3 Film above N Néel temperature induced by forming a junction with Fe_2O_3 Layer: First-principles and monte-carlo study, IEEE Trans. Magn. 50 (2014) 3–6. doi:10.1109/TMAG.2014.2324014.

[24] Y. Kota, H. Imamura, M. Sasaki, Effect of lattice deformation on exchange coupling constants in Cr_2O_3, J. Appl. Phys. 115 (2014) 17D719. doi:10.1063/1.4865780.

[25] Y. Kota, H. Imamura, M. Sasaki, Strain-induced Néel temperature enhancement in corundum-type Cr_2O_3 and Fe_2O_3, Appl. Phys. Express. 6 (2013) 4–8. doi:10.7567/APEX.6.113007.

[26] Y. Kota, Y. Yoshimori, H. Imamura, T. Kimura, Enhancement of magnetoelectric operating temperature in compressed Cr_2O_3 under hydrostatic pressure, Appl. Phys. Lett. 110 (2017) 042902. doi:10.1063/1.4975000.

[27] S.P. Pati, N. Shimomura, T. Nozaki, T. Shibata, M. Sahashi, Néel temperature of Cr_2O_3 in Cr_2O_3/Co exchange-coupled system: Effect of buffer layer, J. Appl. Phys. 117 (2015) 17D137. doi:10.1063/1.4917263.

[28] C. Sun, Z. Song, A. Rath, M. Street, W. Echtenkamp, J. Feng, C. Binek, D. Morgan, P.M. Voyles, Local Dielectric Breakdown Path along c -Axis Planar Boundaries in Cr_2O_3 Thin Films, Adv. Mater. Interfaces. (2017) 1700172. doi:10.1002/admi.201700172.

[29] S. Mu, A.L. Wysocki, K.D. Belashchenko, Effect of substitutional doping on the Néel temperature of Cr_2O_3, Phys. Rev. B. 87 (2013) 54435. doi:10.1103/PhysRevB.87.054435.

[30] M. Street, W. Echtenkamp, T. Komesu, S. Cao, P. a. Dowben, C. Binek, Increasing the Néel temperature of magnetoelectric chromia for voltage-controlled spintronics, Appl. Phys. Lett. 104 (2014) 222402. doi:10.1063/1.4880938.

[31] J.J. Rehr, J.J. Kas, F.D. Vila, M.P. Prange, K. Jorissen, Parameter-free calculations of X-ray spectra with FEFF9., Phys. Chem. Chem. Phys. 12 (2010) 5503–5513. doi:10.1039/b926434e.

[32] R. F. Egerton, Electron Energy-Loss Spectroscopy in the Electron Microscope, Springer, New York, 1996. doi:10.1007/978-1-4615-6887-2.

[33] G. Yang, G. Möbus, R.J. Hand, Cerium and boron chemistry in doped borosilicate glasses examined by EELS, Micron. 37 (2006) 433–441. doi:10.1016/j.micron.2005.12.002.

[34] H. Sauer, R. Brydson, P.N. Rowley, W. Engel, J.M. Thomas, Determination of coordinations and coordination-specific site occupancies by electron energy-loss spectroscopy: An investigation of boron-oxygen compounds, Ultramicroscopy. 49 (1993) 198–209. doi:10.1016/0304-3991(93)90226-N.

[35] C. Souche, B. Jouffrey, G. Hug, M. Nelhiebel, Orientation sensitive EELS-analysis of boron nitride nanometric hollow spheres, Micron. 29 (1998) 419–424. doi:10.1016/S0968-4328(98)00030-4.

[36] H.K. Schmid, Phase Identification in Carbon and BN Systems by EELS, Microsc. Microanal. Microstruct. 6 (1995) 99–111. doi:10.1051/mmm:1995110.

[37] S.B. Zhang, J.E. Northrup, Letters 21, Phys. Rev. Lett. 67 (1991) 2339–2342.

[38] R.M. Jacobs, J.H. Booske, D. Morgan, Intrinsic defects and conduction characteristics of Sc_2O_3 in thermionic cathode systems, Phys. Rev. B. 86 (2012) 54106. doi:10.1103/PhysRevB.86.054106.

[39] M.P. Oxley, S.J. Pennycook, Image simulation for electron energy loss spectroscopy, Micron. 39 (2008) 676–684. doi:10.1016/j.micron.2007.10.020.

[40] D.O. Klenov, S. Stemmer, Contributions to the contrast in experimental high-angle annular dark-field images, Ultramicroscopy. 106 (2006) 889–901. doi:10.1016/j.ultramic.2006.03.007.

[41] N.D.M. Hine, K. Frensch, W.M.C. Foulkes, M.W. Finnis, Supercell size scaling of density functional theory formation energies of charged defects, Phys. Rev. B - Condens. Matter Mater. Phys. 79 (2009) 1–13. doi:10.1103/PhysRevB.79.024112.

[42] Y.-L. Lee, J. Kleis, J. Rossmeisl, D. Morgan, Ab initio energetics of $LaBO_3$ (001) (B = Mn, Fe, Co, and Ni) for solid oxide fuel cell cathodes, Phys. Rev. B. 80 (2009) 224101. doi:10.1103/PhysRevB.80.224101.

[43] P. J. Linstrom and W. G. Mallard, NIST chemistry WebBook, National Institute of Standards and Technology, Gaithersburg, 2003. http://webbook.nist.gov/chemistry/.

[44] L. Wang, T. Maxisch, G. Ceder, Oxidation energies of transition metal oxides within the GGA+U framework, Phys. Rev. B. 73 (2006) 195107. doi:10.1103/PhysRevB.73.195107.

[45] T. Nozaki, Y. Shiokawa, Y. Kitaoka, Y. Kota, H. Imamura, M. Al-Mahdawi, S.P. Pati, S. Ye, S. Yonemura, T. Shibata, M. Sahashi, Large perpendicular exchange bias and high blocking temperature in Al-doped Cr_2O_3/Co thin film systems, Appl. Phys. EXPRESS. 10 (2017). doi:10.7567/APEX.10.073003.
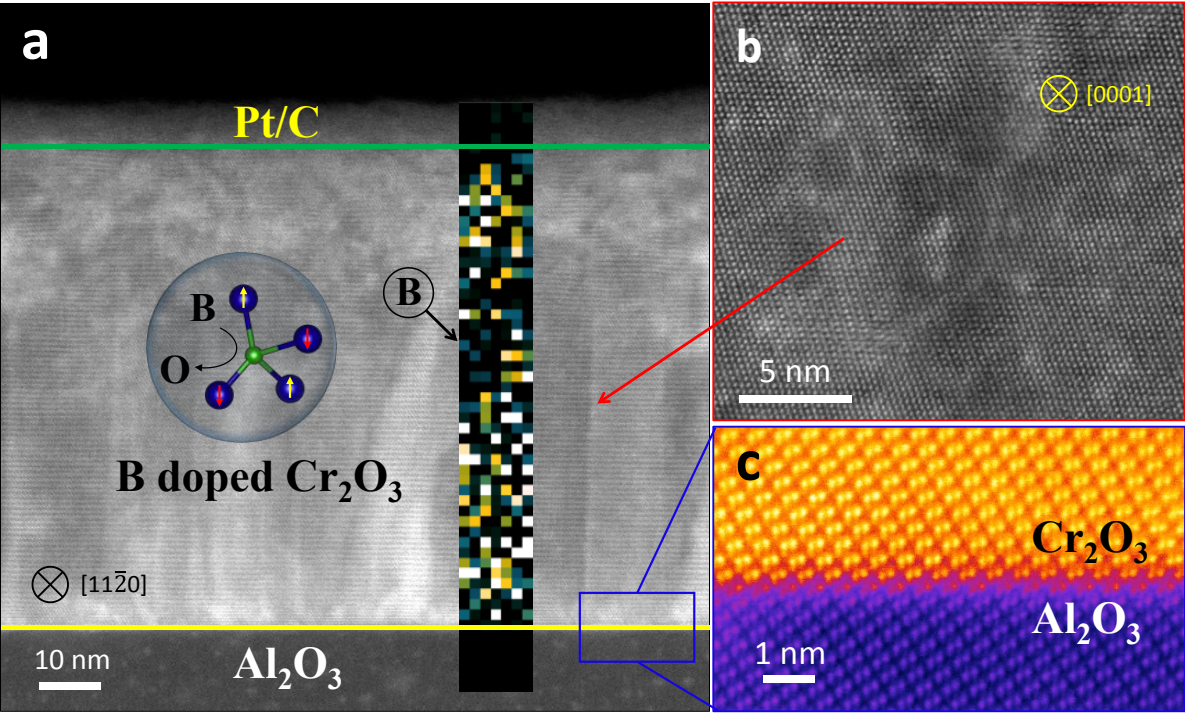
Figures

Figure 1. STEM images of the B doped Cr_2O_3 film. (a) LAADF STEM image showing the flat surface of the Cr_2O_3 film, as well as columnar grains. The inset is the B K edge intensity mapping. (b) Visualizing columnar grains along the plan view direction. (c) HAADF STEM image revealing the epitaxial Cr_2O_3/Al_2O_3 interface and high crystal quality of the Cr_2O_3 film.
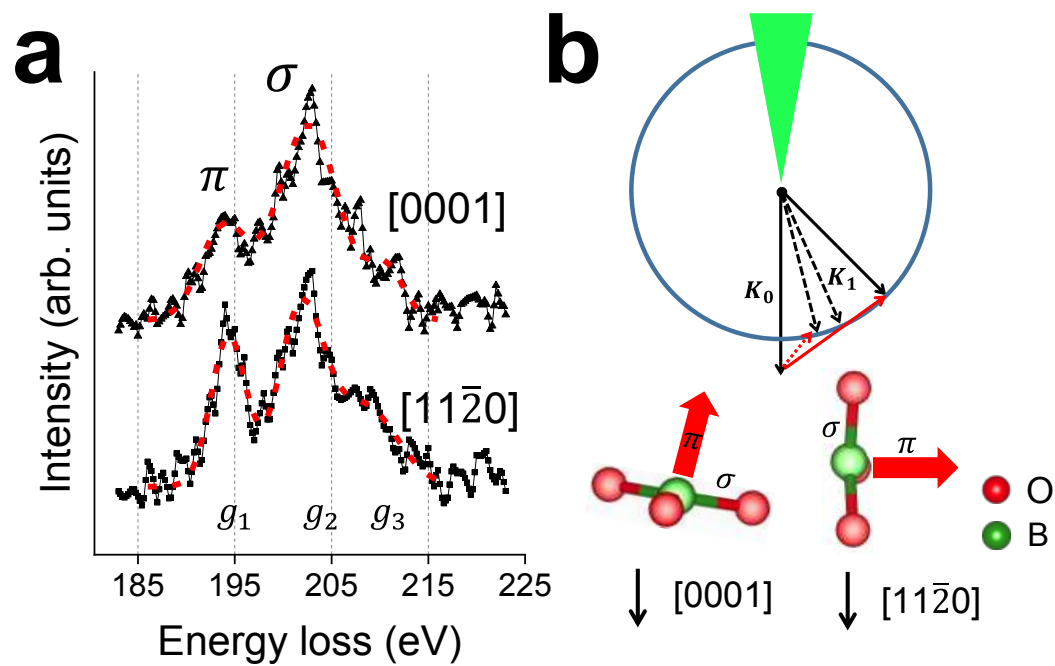
Figure 2. Orientation dependent B K edges EELS. (a) B K edges from plan view (top) and cross section (bottom) zone axis. (b) Schematic illustration showing the projection of electron momentum transfer $\mathbf{q}$ to π bonds with two different sample orientations, i.e, beam along $[11\bar{2}0]$ and [0001] direction.
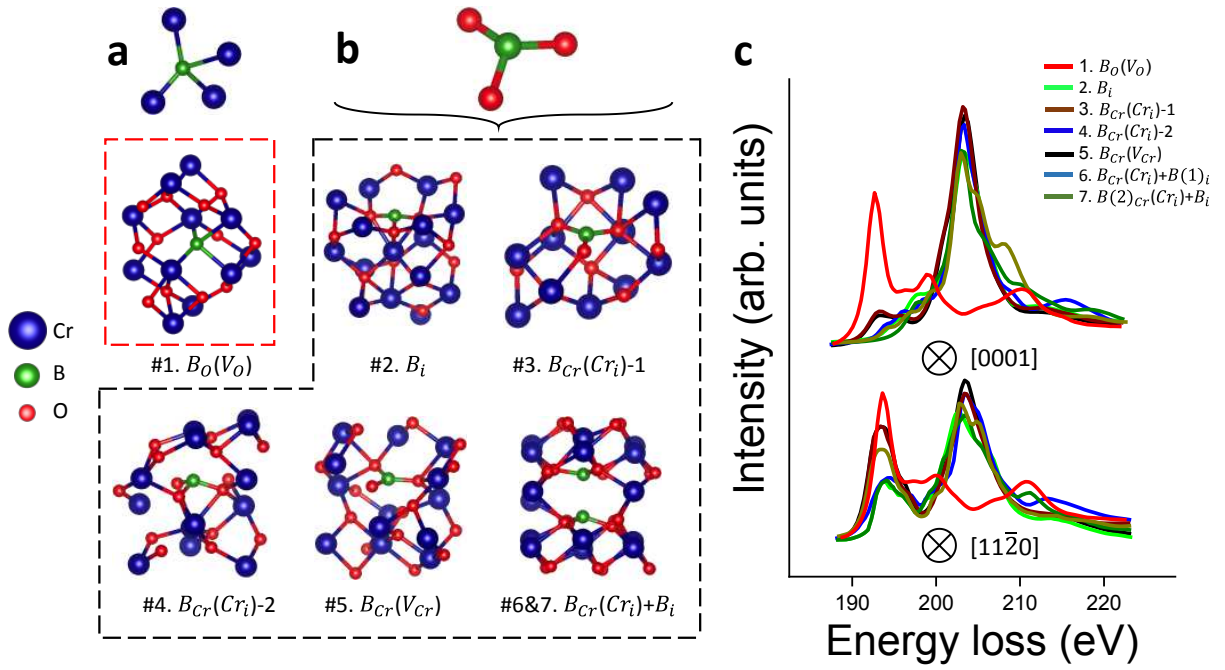
Figure 3. All possible B dopant structures from DFT calculations and corresponding B K edge EELS from multiple scattering simulations. Kroger-Vink notation is used for all the defect types.
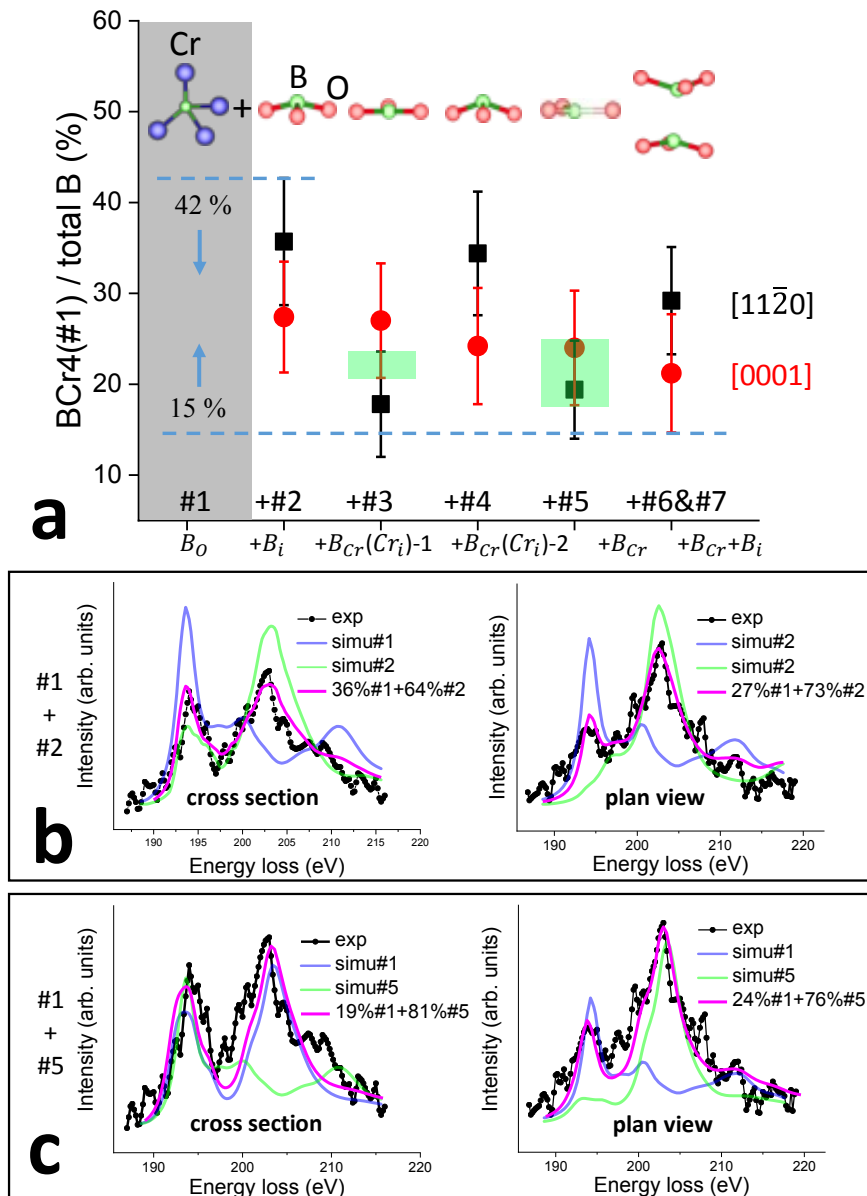
Figure 4. (a) BCr$_4$ / total B (%) from linear combination of simulated BCr$_4$ K edges with BO$_3$ K edges to reproduce the experimental π / σ ratios. (b) Spectra reproduced from BCr$_4$ (#1) and the distorted BO$_3$ (#2). (c) Spectra reproduced from BCr$_4$ (#1) and the planer BO$_3$ (#5).

B nearest Cr ions	#5 Neutral	#5 Charge -1	#5 Charge -2	#4 Charge +3	#4 Charge +1
1	133	187	169	183	255
2	133	129	140	83	283
3	133	143	191	101	73
4	84	83	125	105	87
5	84	124	120	101	94
6	84	83	83	96	76
7	134	133	135	96	88
8	134	139	228	96	89
9	134	86	168	102	105
10	115	109	102	119	103

Table 1. Exchange energies E_n of B nearest Cr neighbors for two lowest energy BO_3 dopant states.
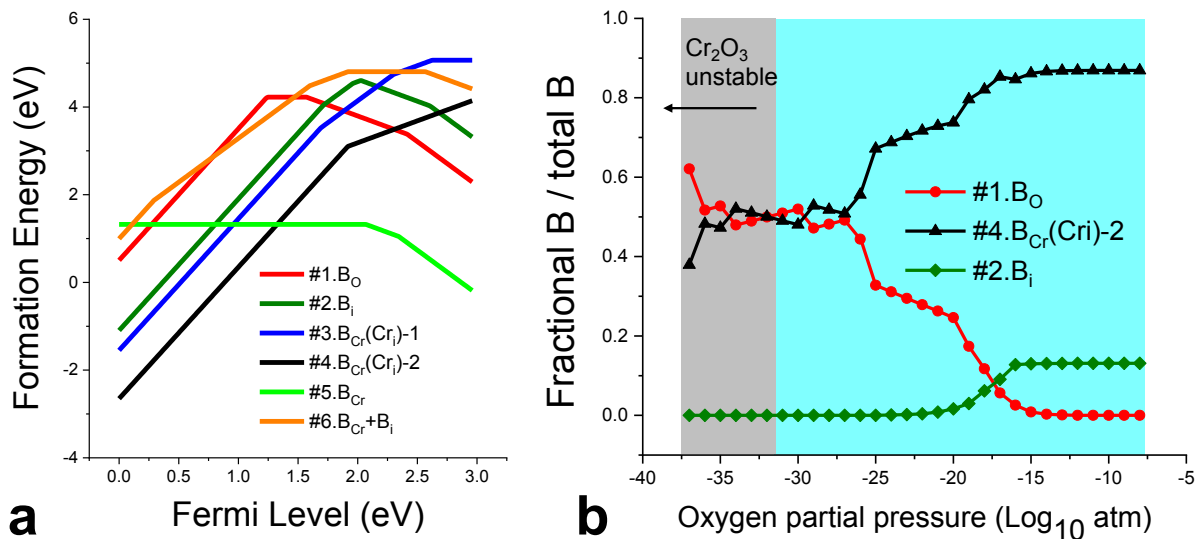

Figure 5. (a) Calculated formation energy as a function of Fermi level for various B dopant structures listed in Figure 3. The temperature is fixed at growth temperature of 700 °C with

complete decomposition of the $B_{10}H_{14}$ background gas. (b) Ratios of each B dopant over total B as a function of oxygen partial pressure.